



HAL
open science

Quick-EXAFS and Raman monitoring of activation, reaction and deactivation of NiCu catalysts obtained from hydrotalcite-like precursors

Aline Ribeiro Passos, Camille La Fontaine, Sandra Helena Pulcinelli, Celso Valentim Santilli, Valérie Briois

► **To cite this version:**

Aline Ribeiro Passos, Camille La Fontaine, Sandra Helena Pulcinelli, Celso Valentim Santilli, Valérie Briois. Quick-EXAFS and Raman monitoring of activation, reaction and deactivation of NiCu catalysts obtained from hydrotalcite-like precursors. *Physical Chemistry Chemical Physics*, 2020, 22 (34), pp.18835-18848. 10.1039/D0CP00380H . hal-03030235

HAL Id: hal-03030235

<https://hal.science/hal-03030235>

Submitted on 13 Dec 2020

HAL is a multi-disciplinary open access archive for the deposit and dissemination of scientific research documents, whether they are published or not. The documents may come from teaching and research institutions in France or abroad, or from public or private research centers.

L'archive ouverte pluridisciplinaire **HAL**, est destinée au dépôt et à la diffusion de documents scientifiques de niveau recherche, publiés ou non, émanant des établissements d'enseignement et de recherche français ou étrangers, des laboratoires publics ou privés.

ARTICLE

Quick-EXAFS and Raman monitoring of activation, reaction and deactivation of NiCu catalysts obtained from hydrotalcite-like precursors

Received 00th January 20xx,
Accepted 00th January 20xx

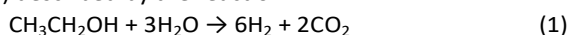
DOI: 10.1039/x0xx00000x

Aline Ribeiro Passos,^{*a,b} Camille La Fontaine,^a Sandra Helena Pulcinelli,^c Celso Valentim Santilli^c and Valérie Briois^{*a}

The understanding of phase transformation upon activation, reaction and deactivation of catalysts is of prime importance for tailoring catalysts with better performances. Herein we combined Quick-EXAFS and Raman spectroscopies *in operando* conditions through the monitoring of reaction products by mass spectrometry in order to study in depth active species and deactivating ones for Ethanol Steam Reforming reaction. Quick-EXAFS data analyzed by multivariate analysis allows one to determine the nickel and copper species involved during the activation of a Ni-Cu hydrotalcite-like precursors. Upon reaction and regeneration monitoring, Raman spectroscopy combined with mass spectrometry highlights the side products formed upon ESR leading to the formation of amorphous coke species encapsulating active metallic species and inducing catalyst deactivation. The coke encapsulation of active species was demonstrated by the simultaneous observation of oxidation of nickel and copper as soon as the amorphous coke was burnt by the oxidative regeneration treatment. Formation of filamentous coke species is also confirmed as causing little impact in catalyst deactivation.

Introduction

Nickel and copper based catalysts are used in a huge number of reactions involving ethanol conversion which can provide building block chemicals such as hydrogen, ethylene, propylene and higher hydrocarbons usually obtained from cracking process of petroleum.^{1,2} Ethanol steam reforming (ESR) described by the reaction:



and leading to the formation of H₂-rich gas is a potential candidate for on-board H₂ production to feed proton-exchange membrane fuel cells for power generation in automobiles.³ Nickel catalysts favor ESR towards the formation of H₂ but also several parallel reactions, leading to fast catalyst deactivation by carbonaceous deposits,⁴ whereas copper ones mainly dehydrogenate ethanol to acetaldehyde.⁵ For those reactions, active species are nanometer-sized metallic particles obtained by reduction of oxidic precursors. The combination of copper and nickel in bimetallic systems leads to several benefits during activation such as an increase of nickel reducibility and improvement of catalyst stability upon reaction conditions.^{6,7}

Hydrotalcite-like precursors are used for bimetallic catalyst preparation regarding their capability to be decomposed upon heating to nanometer-sized mixed oxide phases with high chemical homogeneity.^{8–10} Hydrotalcite-like materials is a family of layered crystal structure similar to brucite, Mg(OH)₂, also called Layered Double Hydroxides (LDH) in which divalent metal atoms such as magnesium, nickel, copper or zinc are partially replaced by trivalent ones such as aluminum, gallium or manganese.¹¹ This aliovalent substitution leads to positively charged layers counter-balanced by anions located in interlayer galleries, such as CO₃²⁻, NO₃⁻, Cl⁻ or SO₄²⁻. The LDH obtained by a one-pot sol-gel route in which gelation is driven by chloride-assisted epoxide rupture exhibited specific surface areas at least 10% higher than those prepared by conventional co-precipitation route^{12–14} The high nucleophilicity of chloride is mandatory in this sol-gel route since lower nucleophilic anions such as NO₃⁻ or SO₄²⁻ did not result in gel formation.¹⁵ The conventional activation pathway of LDH precursor catalysts involves a preliminary calcination where metal oxide phases M²⁺O and M²⁺M³⁺₂O₄ are formed before to be reduced under H₂ atmosphere.^{3,16} Calcination permits to decompose the layered structure and to get rid of intercalated anions.¹⁷ The presence of chloride anions on the LDH prepared by the sol-gel route complicates the LDH decomposition leading to the formation of transitory phases containing anionic species rather than only metal oxide phases.¹⁵ For instance, we reported by X-ray absorption spectroscopy (XAS) the formation of Cu¹⁺Cl_x-like phases at the early stages of calcination under static air atmosphere (T≈200–300°C) of ZnCuAl LDH synthesized with chloride salts.¹⁸ At higher temperature, those

^a SOLEIL synchrotron, L'Orme des Merisiers, BP48, 91192 Gif-sur-Yvette, France

^b Brazilian Synchrotron Light Laboratory (LNLS), Brazilian Center for Research in Energy and Materials (CNPEM), 13083-970, Campinas, SP, Brazil.

^c Chemistry Institute of the São Paulo State University, UNESP, 14800-060, Araraquara, SP, Brazil

† Footnotes relating to the title and/or authors should appear here.

Electronic Supplementary Information (ESI) available: [details of any supplementary information available should be included here]. See DOI: 10.1039/x0xx00000x

$\text{Cu}^{1+}\text{Cl}_x$ -like phases have been further reduced into metallic copper. This last finding inspired us to test a new activation procedure in which the decomposition/activation of the LDH precursors is carried out in a 2-step process with a first oxidative LDH decomposition by heating under synthetic air, followed by a reductive step under H_2 . As copper chloride species can be used as catalysts in the formation of H_2 by water splitting according to the so-called thermochemical Cu-Cl cycle,¹⁹ it appears of prime importance to optimize the 2-step activation procedure in order to get rid of copper chloride phases before to start ESR reaction since the latter involved as reactants not only ethanol but also water as shown in reaction (1). For this purpose, XAS appears as a powerful technique for gaining insights on the decomposition product kinetic and formation of active phases.

On the other hand, producing highly stable catalysts is a major challenge in catalyst science and engineering. During ESR, carbon formation may take place *via* several reactions, such as ethanol dehydration to ethylene, Boudouard reaction and methane decomposition.^{20,21} The high temperatures required for the reaction favor the formation of large quantities of carbon deposits decreasing the catalytic activity.²⁰ Manukyan *et al.*²² showed that $\text{Ni}/\text{Al}_2\text{O}_3$ catalysts derived from LDH exhibit highly dispersed Ni^0 nanoparticles and higher resistance to deactivation during ESR compared to a catalyst prepared by impregnation route. However formation of carbonaceous deposits cannot be prevented causing numerous problems in chemical plants as catalyst replacement and process shutdown.²³ New technologies are required to regenerate deactivated catalysts in economic, recyclable and environmentally friendly way.

We have already reported that the simultaneous monitoring of ESR reaction/regeneration cycles by Quick-EXAFS and Raman spectroscopy can be efficiently used for proposing regeneration protocols carried out at the same temperature than the ESR reaction.^{6,24} This regeneration route involved either the simultaneous use of ESR reactant mixture with the controlled addition of O_2 ²⁴ or the stop of ESR feed to introduce O_2 .⁶ We evidenced that the oxidative regeneration burned coke and partially oxidized metallic M^0 particles. After regeneration, the catalysts were self-reactivated thanks to the hydrogen produced by the ESR reaction (1). Despite a decreasing amount of M^0 species at each reaction-regeneration cycle, we observed that the catalytic activity remained stable. This behaviour was interpreted as resulting from M^0 particle fragmentation related to the so-called Kirkendall effect²⁵ during oxidative treatment of coke encapsulating metallic particles. There are different types of coke which can be formed during ESR, such as amorphous polymeric films (C_a), vermicular filaments (C_v) and graphitic crystalline platelets (C_c), which do not impact similarly the catalytic activity.²³ Amorphous coke is described in the literature as being the most deactivating one by blocking the access of the reactants on the active sites.²¹ Through an in-depth evaluation of products formed upon time of stream (TOS) under different reaction conditions, it has been

proposed that the formation of amorphous coke is associated to high content of ethylene and acetaldehyde side-products.²¹

In this paper, we studied in depth by multivariate curve resolution with alternating least square (MCR-ALS) fittings of the time resolved XAS data^{26,27} the activation of a bimetallic NiCu catalyst prepared from LDH precursors and the in-line regeneration of catalyst deactivated by coke deposits during ESR reaction. The objectives in this paper were 3-fold:

(i) Optimize the activation route based on pre-oxidative treatment followed by reductive one directly applied to the NiCu-based LDH precursors synthesized by a one-pot sol-gel route involving chloride salts as reactants.¹³ We demonstrated how unique is the Quick-EXAFS spectroscopy for monitoring the 2-step activation of NiCuAl-LDH precursors for preparing efficient bimetallic NiCu catalyst for ESR. In particular we highlighted how powerful is the MCR-ALS method to isolate and identify the intermediate species formed during activation.

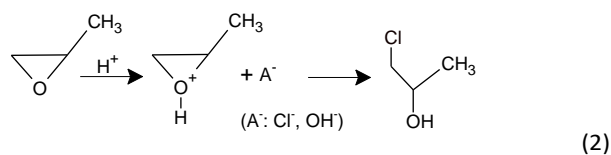
(ii) Then, we used also the time resolution available on Quick-EXAFS beamlines installed on third Synchrotron generation facility like SOLEIL to study the reactivity of metallic nanoparticles freshly formed by activation by applying alternating oxygen and hydrogen pulses in the reactor feed. Pulsing treatments carried out on monometallic catalysts based either on nickel and copper were compared to the treatment carried out on the bimetallic one in order to evaluate the hypothesis of the formation of Cu-rich core and Ni-rich shell particles.

(iii) Finally, taking advantage of the simultaneous monitoring of ESR reaction/regeneration cycles by Quick-EXAFS and Raman spectroscopy, we contributed to the discussion found in the literature first about the relationship between the nature of coke formed upon TOS and deactivation and second about the nature of coke formed and concentration of side-products. To the best of our knowledge, this should be the first direct evidence of the interpretations made in the literature on the basis of separate *ex situ* characterizations.²¹

Experimental

Catalysts Preparation

Ni-Cu-Al LDH precursor was produced by sol-gel route according to a previously described method.⁶ Briefly, for the synthesis of the bimetallic NiCu catalyst, first, 0.70 g of $\text{NiCl}_2 \cdot 6\text{H}_2\text{O}$, 0.13 g of $\text{CuCl}_2 \cdot 2\text{H}_2\text{O}$ and 1.78 g of $\text{AlCl}_3 \cdot 6\text{H}_2\text{O}$ were dissolved in a mixture of 4.52 mL of H_2O and 3.45 mL of $\text{CH}_3\text{CH}_2\text{OH}$ at 25 °C under stirring for 10 min. Then 2.58 mL of propylene oxide (PO) was added to increase the pH from 0 to 3 and promote the gelation. PO acts as H^+ scavenger through the protonation of the epoxide oxygen and subsequent ring-opening reactions and Cl^- complexation through the formation of nucleophilic anionic conjugate base²⁸ (reaction 2).



A homogeneous gel was prepared with the molar composition: $x\text{NiCl}_2 \cdot 6\text{H}_2\text{O} : y\text{CuCl}_2 \cdot 2\text{H}_2\text{O} : 1\text{AlCl}_3 \cdot 6\text{H}_2\text{O} : 34\text{H}_2\text{O} : 8\text{CH}_3\text{CH}_2\text{OH} : 5\text{PO}$, where $x + y = 0.5$ with $x = 0.4$ and $y = 0.1$ for the bimetallic catalyst and $x = 0.5$, $y = 0.5$ for the monometallic catalysts to keep a constant metal fraction. An additional monometallic catalyst was prepared with $y = 0.1$. The samples were named according to the molar composition of M^{2+} salt: $\text{Ni}_{0.4}\text{Cu}_{0.1}$, $\text{Ni}_{0.5}$, $\text{Cu}_{0.5}$ and $\text{Cu}_{0.1}$ respectively. The wet gel was dried at 50°C . The loading of M^{2+} in the catalyst was 33 wt%.

Catalyst Activation and Reaction Conditions

The catalyst activation of the LDH precursors was performed at atmospheric pressure using a Lyttle-type reactor²⁹ with a 2mm thick sample holder loaded with 21 mg of the sample according to a 2-step process involving the precursor heating under two different gaseous atmospheres. The temperature and the gas atmosphere protocol (Fig. S1, ESI) are based on the LDH thermal decomposition steps evidenced by thermogravimetric analysis (Fig. S2, ESI). First a pre-calcination under synthetic air was carried out by heating the LDH precursors from room temperature (RT) to 210°C at 5°C min^{-1} , and then after a purge of 5 min under He, the samples were further heated up to 500°C at $10^\circ\text{C min}^{-1}$ under 5% of H_2/He in order to form the metallic nanoparticles. We hereafter denote the pre-calcination, as oxidative step and the activation under H_2 as reductive step.

At the end of heating ramp, the ESR was carried out at 500°C using an ethanol/water reactant mixture at a molar ratio of 1/6 and He as carrier gas passing through a saturator containing the mixture maintained at constant temperature (45°C). To prevent condensation of liquid reactants and products, the gas inlet and outlet lines were heated up to 100°C . The ethanol conversion and products of reaction were measured using an online quadrupole mass spectrometer (Cirrus, MKS). The gas outlet composition in CO_2 , CH_3CHO , $\text{CH}_3\text{CH}_2\text{OH}$, CO , C_2H_4 , H_2O , O_2 , CH_4 and H_2 was calculated from the m/z signal collected for 44, 33, 31, 28, 26, 17, 16, 15 and 2, respectively.

Regeneration of coked catalysts

After ESR reaction and abundant formation of coke, the bimetallic catalyst was regenerated by introducing 20 mL min^{-1} of 5% O_2/He at 500°C for 1 h. Then, the $\text{EtOH}/\text{H}_2\text{O}$ reactants carried by gaseous He was supplied again in the reactor for running the ESR reaction for 1 h. The regeneration was monitored simultaneously by Quick-EXAFS, Raman spectroscopy and Mass Spectrometry (MS). Raman measurements were carried out using a RXN1 spectrometer from KOSI (Kaiser Optical Systems, Incorporation) equipped with diode pumped solid state laser (532 nm) and a long working distance x10 objective (150 mm). The window of the

reactor facing the laser was a $25\ \mu\text{m}$ thick mica window. During the first reaction, one spectrum was recorded every 5 min with integration time of 3 min, then during regeneration and subsequent reaction, spectra were measured continuously with integration time of 1.5 min.

Pulse Treatments

Activated catalysts with different compositions using the 2-step process were submitted to alternate pulses using 5% O_2/He (20mL/min) and 10% H_2/He (20mL/min) with 5 s of He flow (20 mL/min) between each pulse. The activation and pulse treatment were carried out in a capillary flow reactor (outer diameter 1.2 mm, wall thickness $20\ \mu\text{m}$) heated with a gas blower. This set-up is optimized to reduce the gas line length in order to have an efficient fast exchange of atmosphere in the reactor. For the pulse treatment, the catalyst precursors were diluted with diamond with a granulometry ranged between $20\text{-}30\ \mu\text{m}$. About 1.75 mg of catalyst was loaded in the capillary, regardless the catalyst composition.

Quick-EXAFS measurements and analysis

Quick-EXAFS measurements at the Cu (8979 eV) and Ni (8333 eV) K edges were recorded simultaneously at the ROCK beamline (SOLEIL synchrotron)³⁰ using the Si(111) Quick-EXAFS monochromator with the main goniometer aligned at 12.80° and an oscillation amplitude of 2.6° in order to cover the extended energy range from 8170 to 9800 eV. Mirrors with a B_4C coating and a grazing incidence of 2.8 mrad with respect to the pink and monochromatic beams were used for harmonic rejection. Data were collected in transmission mode using 3 ionization chambers filled with nitrogen, the two first ionization chambers are used for measuring the sample transmission whereas the second and third ones are used for collecting the signal of nickel and copper reference foils. Oscillation frequency of the crystal was chosen at 2Hz giving rise per second of 2 spectra collected with ascending Bragg angles and 2 spectra collected with descending Bragg angle. In order to improve the Signal to Noise ratio, 20 spectra recorded successively were merged leading to a time resolution of 10 s between each presented spectrum. Normalization of the XAS spectra was performed using the Python normal_gui graphical interface developed at the beamline for the fast handling of the Quick-XAS data.³¹

The speciation of the different Ni and Cu species was determined by a multivariate data analysis, the so-called Multivariate Curve Regression with Alternating Least Square (MCR-ALS) method.³² This method allows for isolating from a data containing the spectra of an evolving mixture of products the spectrum of each pure species participating to the reaction and its concentration profile. To this purpose, the normalized experimental XAS spectra were organized in ascending reaction time in a matrix D. In agreement with the Beer-Lambert law at which XAS obeys, a bilinear decomposition of the matrix D could be done into the matrix containing the concentration of the pure components (C) and the matrix

containing the normalized XAS spectra of the pure components (S^T), according to the relation:

$$D = C \cdot S^T + E \quad (3)$$

with E the matrix containing the experimental noise. The MCR-ALS algorithm calculates a mathematical set of concentrations and spectra allowing one to explain most of the variance of the experimental data set D. Matrices C and S^T are determined alternately by minimizing the differences between D and the product $C \cdot S^T$ during a series of loops which are stopped when the convergence criterion defined by the user is reached. In order to suppress rotation ambiguities in the MCR-ALS solutions, physically and chemically meaningful constraints were imposed during the minimization, like the non-negativity of the matrix of pure spectra S^T , the non-negativity of the matrix of concentrations C and the closure relation on the concentrations which obliges for a given chemical element that the sum of the concentrations of all the species involved in the reaction is constant. Prior to MCR-ALS minimization, Principal Component Analysis (PCA) evaluation³³ is carried out on the same data set in order to determine the number of components which are necessary to explain most of the variance contained on the data set. Details about methods used to evaluate the most appropriate number of components, as Scree plot and Score Trajectory, can be found in^{31,34}. The MCR-ALS minimization on the Quick-XAS data presented herein was carried out using the MCR-ALS GUI 2.0 developed by Roma Tauler and his group on the Matlab® platform.³⁵ An initial guess of the matrix of concentration for the ALS minimization was performed using the Evolving Factor Analysis (EFA) method.³⁶

Ex situ characterization

Transmission electron microscopy (TEM) images were obtained using a JEM 2100 (JEOL) instrument operating at 200 kV (point resolution 0.25 nm). For TEM analyses the catalyst powder was dispersed ultrasonically in ethanol and then transferred as a suspension to a carbon-coated copper grid. The crystalline phases present in the LDH precursor were characterized by XRD using a Bruker D2 Phaser diffractometer with $\text{CuK}\alpha$ radiation. BET specific surface area was determined by nitrogen adsorption desorption using a Micromeritics ASAP2010 instrument. Prior to the measurements, the LDH precursor was degassed at 110 °C for 12 h under vacuum of 10 mPa. The Brunauer-Emmett-Teller (BET) equation was used to calculate the specific surface area.³⁷

Results and discussion

Activation of as-prepared NiCu-LDH precursors

The observation in the XRD patterns (Fig. S3, ESI) of peaks at 2θ values equal to 11.4°, 22.8°, 35.2° and 62.5° allows one to confirm the formation of LDH in the as-synthesized sample since those peaks correspond to the (003), (006), (012) and (113) reflections characteristic of hydrotalcite.⁸ The basal distance calculated from (003) and (006) peak positions was 7.76 Å, in good agreement with the value observed for

chlorine intercalated LDH.³⁸ The sol-gel synthesized LDH presents high BET surface area, 194 m^2g^{-1} .

In a previous publication,⁶ we investigated the ESR activity of NiCu catalysts prepared from the same LDH precursors studied herein. In that case, the active catalysts were obtained through conventional activation process involving first a calcination treatment to decompose at moderate temperature ($T = 500^\circ\text{C}$) the LDH precursors into NiO and CuO and second a heating under H_2 from RT to 500°C with a 3 h of heating at 500°C. We evidenced that despite the long isothermal heating, nickel oxidic species was not fully reduced before starting the ESR reaction letting about 25% to 31% of nickel atoms belonging to oxidic phase depending on the sample composition whereas copper was totally reduced, irrespective of the composition. Herein, we optimize a new activation process in order to improve the reduction of nickel before starting ESR reaction. Abundant literature exists for describing the different stages of thermal decomposition of LDH.^{9,12} The formation of M^{2+}O and $\text{M}^{2+}\text{M}^{3+}_2\text{O}_4$ phases with nanometric sizes is usually reported between 200 to 300°C.¹⁸ Our idea is to introduce H_2 in the gas feed in this temperature range, *i.e.* during the formation of those oxidic nuclei in order to reduce the activation barrier to form reduced species. However, the synthesis route used in the preparation of the LDH precursors intercalated with chloride anions involves organic reagents used to drive homogeneous pH increase of aqueous solutions leading to a homogeneous gelation and LDH formation. As the as-prepared gels still contain organic compounds, they were first decomposed at low temperature during the oxidative step carried out from RT to 210°C, an increasing in the CO_2 m/z signal can be observed due to carbon oxidation (Fig. S4, ESI). The steps supporting the activation of the as-prepared LDH-catalyst used herein are compared to the ones used in the conventional activation process previously used (Fig. S1, ESI).⁶

Fig. 1a and 1b display the XANES spectra recorded at the Ni and Cu K edges during the oxidative and reductive steps of the bimetallic catalyst formation. Clearly no isobestic points are observed for both elements indicating that more than 2 species for each data set are involved during the activation of the as-prepared LDH-catalyst. Strong modifications of the shape of the XANES spectra are observed at both edges starting from the RT-spectra characteristic of the LDH local order structure to the spectra measured at 500°C characteristic of metallic species. The RT spectra display a pre-edge with very low intensity and an intense white line with a maximum at 8351.8 eV at the Ni K edge and 8996.5 eV at the Cu K edge, both features being well-known fingerprints of octahedral symmetry around 3d cation as expected for divalent cations embedded in the LDH sheets.³⁹ Upon the 2-step activation process, the white line strongly decreases and the energy position of the rising edge shifts at lower energy. However, as displayed in Fig. 1c important differences are observed between the nickel and copper edges dependency with the reactor temperature for the position of the rising edge at absorbance equal 0.3. An important shift of the Ni K edge rising position occurs around 357°C whereas successive decrease of the energy of the edge is observed for the Cu K

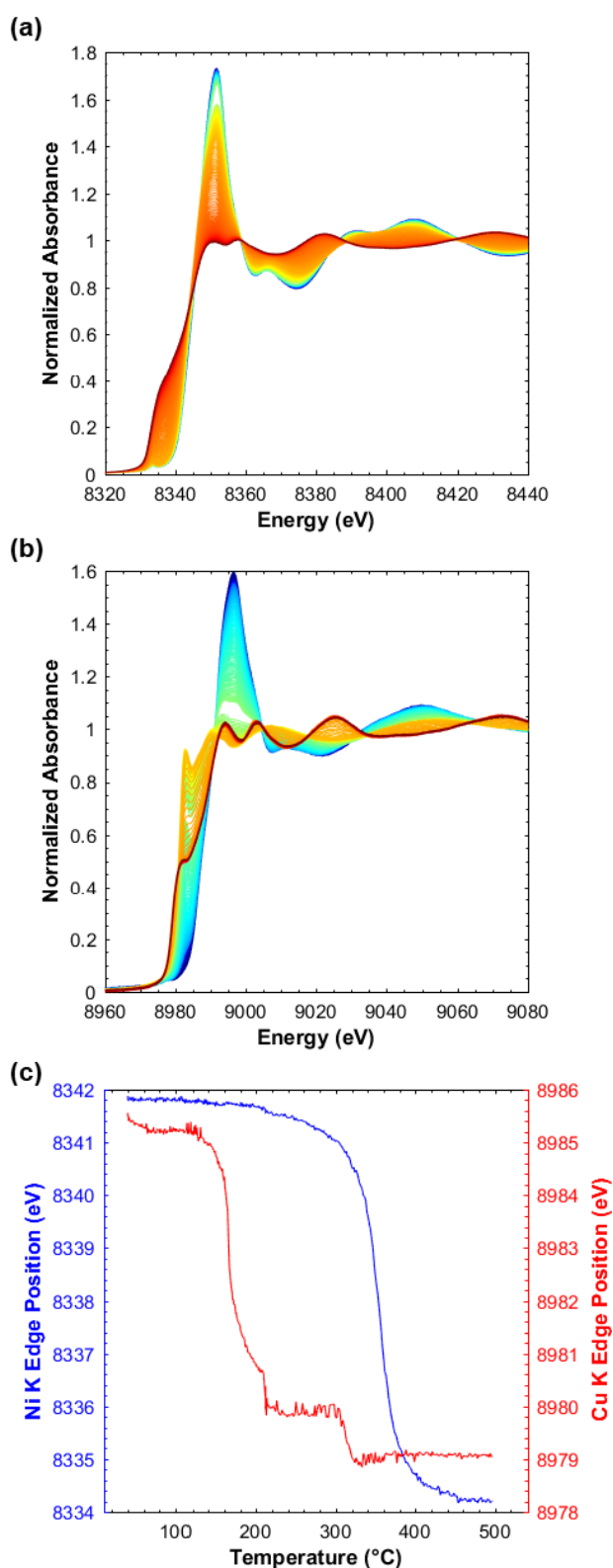


Fig. 1 (a) Ni K edge XAS data and (b) Cu K edge XAS data recorded upon the 2-step activation of the NiCu-LDH-precursors by heating the sample under air from RT (deep blue curves) to 210 °C and then under 5% H₂ up to 500 °C (deep red curves). (c) Comparison of the position of rising edge measured at absorbance equal to 0.3 for the Ni and Cu K edges data as a function of the activation temperature.

edge data, the first one during the oxidative step at 166 °C and a second one during the reductive step around 313 °C. Considering the observed energy shifts, this corresponds to the characteristic temperature of reduction of Cu²⁺ into Cu⁺ and then into Cu⁰, respectively.⁶

The number of components involved during the Quick-EXAFS monitoring of the activation of the bimetallic NiCu catalysts first determined by PCA revealed that 3 components are required at the Ni K edge (Fig. S5, ESI) for explaining most of the variance contained in the data. The MCR-ALS minimization considering 3 components for the data set presented in Fig. 1a is reported in Fig. S6 of Supplementary Information. The first component is the pristine LDH oxide, the third one is identified as the Ni⁰ metallic species whereas the second and intermediate one is a mixture of NiO and NiAl₂O₄ nanophases which cannot be separated by MCR-ALS analysis due to correlated variations in the concentrations of both species. Similar behaviours were described for Zn-based LDH.¹⁸ The XANES spectra of the 3 components isolated at the Ni K edge are displayed in Fig. 2a whereas the EXAFS spectra and associated Fourier Transforms are presented in Fig. S7 of Supplementary Information. The PCA evaluation (Fig. S8, ESI) of the number of components involved in the data set recorded during the Cu K edge monitoring of the 2-step activation of the NiCu LDH precursors does not permit to decide between 3 or 4 components. The right number of components for Cu K edge data was found considering the results obtained for the calcination of the same LDH precursor under synthetic air up to 500 °C (Fig. S9, ESI), insofar as the onset of calcination is common with the oxidative step and therefore shares common intermediates. At the Cu K edge, the calcination of Cu-based LDH precursors (Fig. S9, ESI) leads first to a Cu⁺ species identified i) by its characteristic XANES spectrum and ii) by the least-square simulation of its EXAFS spectrum as being a CuCl₂⁻ species⁴⁰ before itself to be transformed into an atacamite-like species, with formula Cu₂(OH)₃Cl. Details about the simulation and identification of the species can be found in Supplementary Information (Fig. S10-S11 and Table S1, ESI). At the temperature at which air atmosphere is exchanged by H₂, the LDH phase, the CuCl₂⁻ and the atacamite-like species coexist. This finding justifies the use of 4 components for the multivariate analysis of the Cu K edge data recorded during the 2-step activation process insofar as reductive atmosphere will reduce those 3 species into Cu⁰.

Nevertheless, in the temperature range used for the oxidative activation step, the atacamite-like species is present at a quite low percentage (<15%), thus the minimization of the Cu K edge data recorded during the 2 step activation with 4 components cannot properly isolate the spectrum of the atacamite-like structure. In order to isolate this species, we analysed simultaneously the data recorded for the precursor during the calcination and during the 2-step activation process using the so-called column-wise augmented (CWA) method (Fig. S12 and S13, ESI).⁴¹ The XANES spectra of the 4 components isolated by MCR-ALS of the CWA data set at the Cu K edge are displayed in Fig. 2b whereas the EXAFS spectra and associated Fourier Transforms are presented in Fig. S14

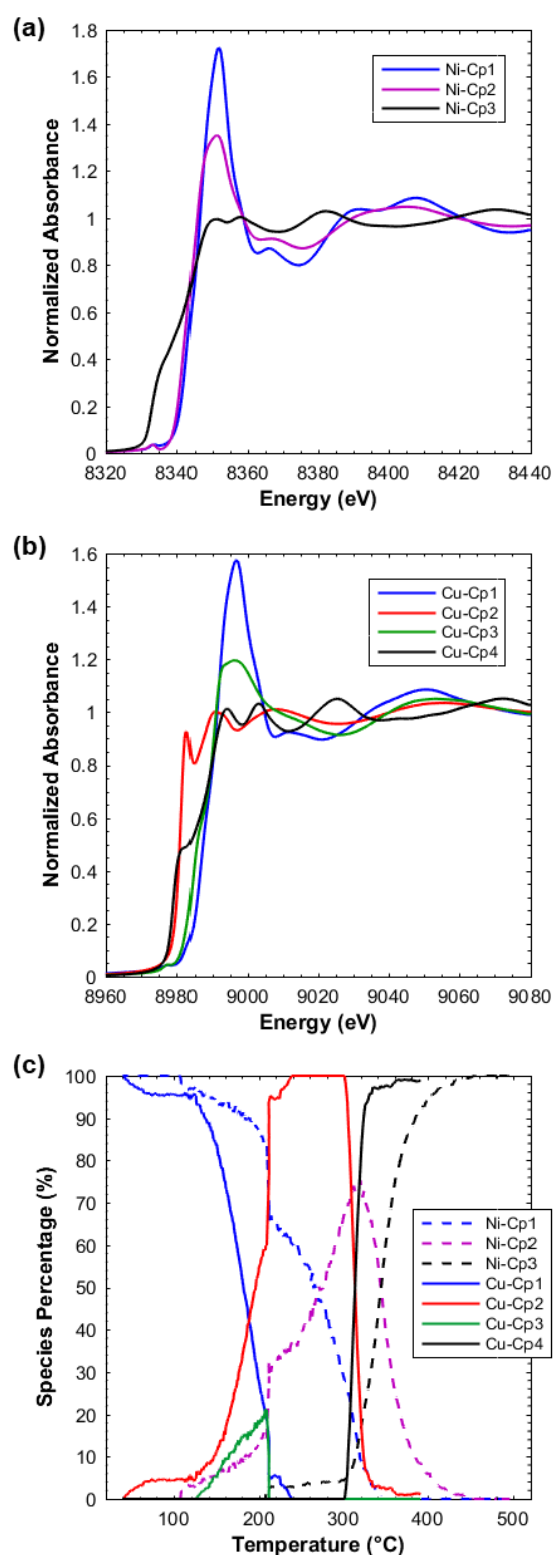


Fig. 2 (a) Ni K edge XANES spectra and (b) Cu K edge XANES spectra of the MCR-ALS components isolated upon the multivariate analysis of the Quick-EXAFS data recorded during the 2-step activation of the NiCu-LDH-precursors. (c) Evolution of the concentration profiles of the MCR-ALS components as a function of the 2-step activation temperature.

(ESI). This allows for extracting the concentration profiles of the Cu-based species presented in Fig. 2c. The evolution of these percentages is compared with the concentration profiles of the Ni-based species. During the purge under He of the reactor between the oxidative step and the reductive one, the acquisition was stopped a couple of seconds but not the chemical transformation. This is responsible for the discontinuity of the profile evolution at 210°C for the species coexisting at this temperature.

As deduced from the variation of the rising edge position of each element (Fig. 1c), the expulsion of copper atoms from the LDH sheets is easier than nickel ones since this occurs around 150°C for Cu against 210°C for Ni. Copper rapidly reacts with the chloride ions located in the intralayer space to mainly form CuCl_2^- and at lower percentage an atacamite-like phase where Cu is still bounded to hydroxyl groups and chlorine ligands. When H_2 is introduced in the reactor at 210°C, the atacamite-like species is immediately reduced into CuCl_2^- . This monovalent Cu species is stable up to 300°C before to be reduced into Cu^0 nanoparticles. Completion of Cu reduction is achieved at 335°C where nearly 100% of Cu^0 is formed. As this temperature corresponds to the onset of reduction of the mixture of NiO and NiAl_2O_4 phases formed upon LDH decomposition at the Ni K edge, we assume that Cu^0 catalyses the decomposition of H_2 adsorbed at the surface of nickel oxidic species supplying active H species for promoting reduction of the nickel oxidic species. 100% of Ni^0 species is formed at 450°C. It is noteworthy that by similar 2-step activation process, complete reduction of the monometallic $\text{Ni}_{0.5}$ -LDH precursor is achieved only at 495°C. The decrease by about 45°C of the temperature of formation of Ni^0 species in the $\text{Ni}_{0.4}\text{Cu}_{0.1}$ bimetallic sample could be explained also by a heterogeneous nucleation of nickel metallic particles over the copper metallic particles early formed leading to the formation of a $\text{Ni}_{0.4}\text{Cu}_{0.1}$ metallic alloy.⁶

Finally the reduction level of nickel is much higher (100%) for the same catalysts using the 2-step activation described herein than the one starting from the reduction from RT to 500°C of pre-calcined catalysts at 500°C⁶ where only 75% of nickel was reduced to Ni^0 after 3 h of isothermal heating at 500°C under H_2 . This result shows that the new activation route optimized herein is more efficient for producing metallic nanoparticles than the conventional ones (Fig. S1, ESI). The MCR-ALS analysis of the data recorded during the Quick-EXAFS monitoring of the 2-step activation process emphasizes that to get rid of the CuCl_x species resulting from the LDH thermal decomposition in presence of chlorine, a temperature higher than 330-350°C is necessary. Considering that higher reaction temperature is used for ESR (450 to 550°C), there is no risk to have spurious contamination of the catalysts by those CuCl_x species, but for ethanol dehydrogenation reaction usually carried out between 250-350°C⁵ and for which Cu-based catalysts are known as efficient the information gained on the copper speciation by Quick-EXAFS/MCR-ALS would be clearly unique for optimizing catalysts for this reaction.

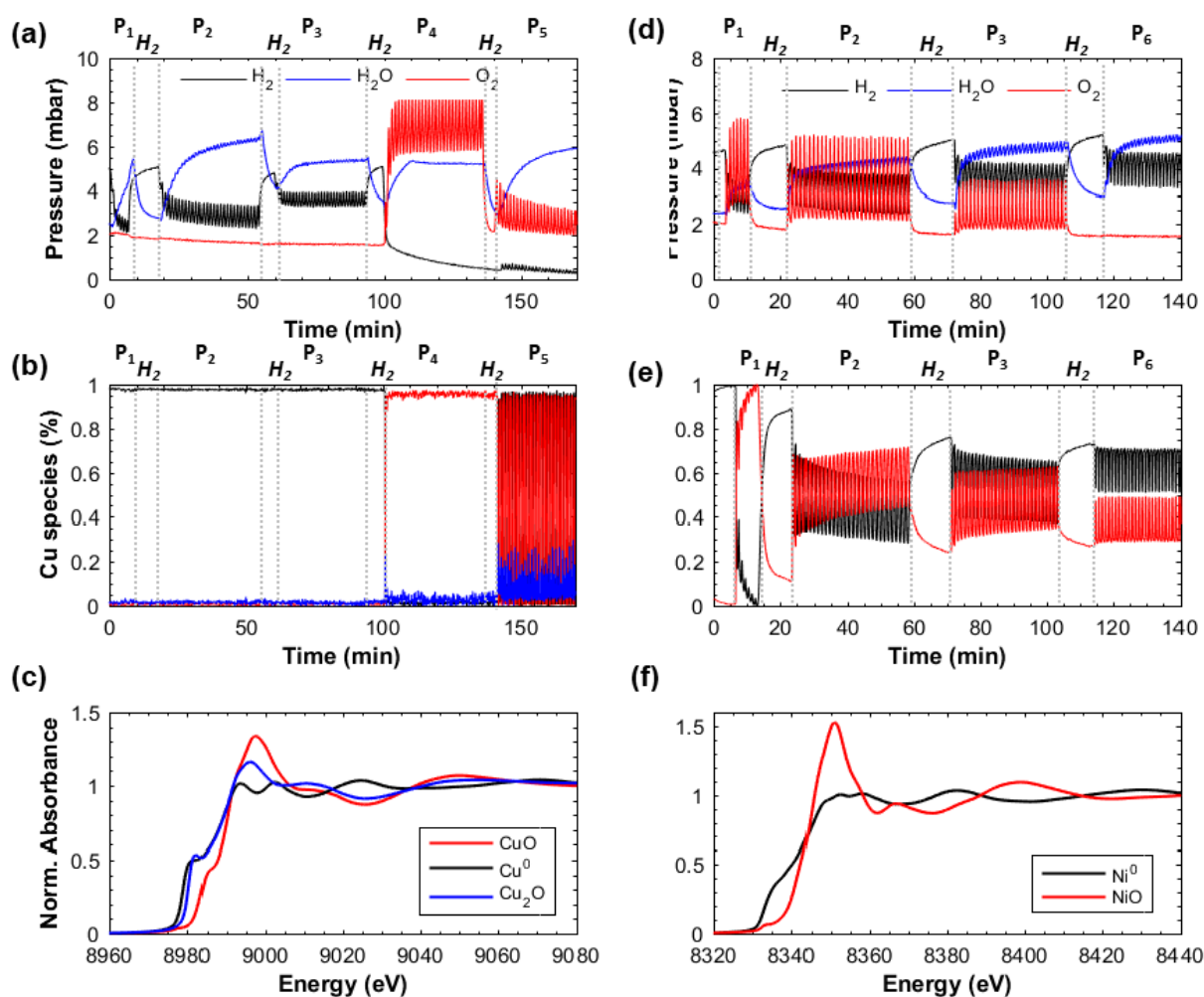


Fig. 3 Evolution of (a) and (d) H_2 , H_2O and O_2 mass signals at the outlet of capillary for different pulse sequences, for the monometallic $\text{Cu}_{0.5}$ and $\text{Ni}_{0.5}$ catalysts, respectively. (b) and (c) Concentration profiles and spectra of Cu species extracted by MCR-ALS for the Quick-EXAFS data recorded during different pulse sequences for the $\text{Cu}_{0.5}$ catalyst. (e) and (f) Concentration profiles and spectra of Ni species extracted by MCR-ALS for the Quick-EXAFS data recorded during different pulse sequences for the $\text{Ni}_{0.5}$ catalyst. The black lines in (b) and (e) are related to the metallic species, the red lines are associated to the divalent oxidic species, CuO and NiO , the blue lines in (b) and (c) are related to Cu_2O . Pulse Sequences: $P_1=20$ s- O_2 /30 s- H_2 , $P_2=20$ s- O_2 /40 s- H_2 , $P_3=15$ s- O_2 /40 s- H_2 , $P_4=40$ s- O_2 /20 s- H_2 , $P_5=30$ s- O_2 /30 s- H_2 and $P_6=10$ s- O_2 /40 s- H_2 .

Stability of metallic particles under cyclic O_2 and H_2 pulses

In order to have a better insight on the composition of the active metallic particles and potential formation of NiCu alloys, we have studied in depth the stability of monometallic $\text{Cu}_{0.5}$, $\text{Ni}_{0.5}$, $\text{Cu}_{0.1}$ and bimetallic $\text{Ni}_{0.4}\text{Cu}_{0.1}$ catalysts prepared from the 2-step activation process under cyclic O_2 and H_2 pulses. Irrespective to the chemical composition of catalyst, complete reduction of metals was achieved at the end of the activation.

Fig. 3 displays for the monometallic catalysts the evolution of concentration profiles determined by MCR-ALS analysis for reduced, Ni^0 and Cu^0 , and oxidized NiO , CuO and Cu_2O , species as a function of the O_2 and H_2 pulse protocol together with the composition of the gas effluents, *i.e.* in O_2 , H_2 , and H_2O at the capillary outlet measured by Mass Spectrometry. It is noteworthy that a blank experiment was carried out on the diamond powder used for dilution in the capillary with the same pulse sequences and MS monitoring (Fig. S15, ESI).

Irrespective to the duration of pulses, the signal of O_2 and H_2 was always detected at the outlet for the blank experiment. Small amount of water was also detected with a signal in phase with H_2 pulses resulting from a few ppm content of H_2O impurity inside the H_2 gas cylinder.

For the $\text{Cu}_{0.5}$ catalyst, no change of oxidation state was observed for alternate pulses with 20 s- O_2 /30 s- H_2 (P_1), 20 s- O_2 /40 s- H_2 (P_2) and 15 s- O_2 /40 s- H_2 (P_3): copper remained at the metallic state. However, contrarily to the MS behaviour observed for the blank experiment, no pulsed O_2 contribution was observed at the cell outlet for the same pulse sequences for the $\text{Cu}_{0.5}$ catalyst suggesting that O_2 is immobilized in the catalytic bed without modifying the copper oxidation state. The increase of O_2 pulse duration to 40 s (P_4) transformed irreversibly Cu^0 into CuO . In that case, the H_2 signal which should be associated to the 20 s of duration does not present a pulsed shape indicating that no enough hydrogen is provided

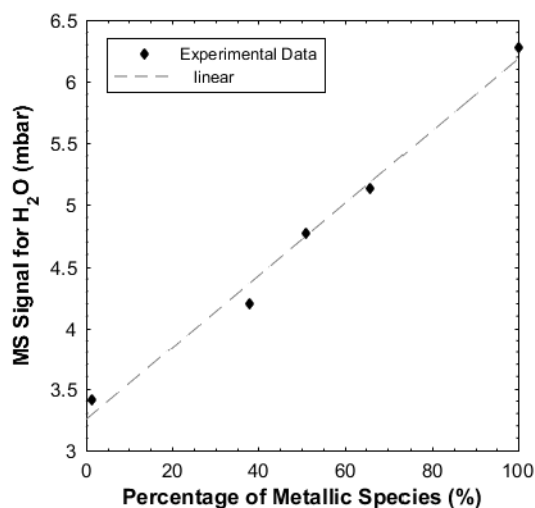


Fig. 4 Correlation of the MS signal recorded for H₂O with the percentage of metallic species obtained on monometallic catalysts.

to the sample for leading to reduction. Finally, a reversible cyclic behaviour with transformation of Cu⁰ into CuO under O₂ pulses and reversible transformation under H₂ pulses was evidenced for the 30 s-30 s pulse sequence (P₅) (Fig. S16, ESI).

At the opposite, the Ni_{0.5} catalyst was very sensitive to the oxidative pulse exposure, with total oxidation of metal at the first series of pulses with duration 20 s-O₂/30 s-H₂ (P₁). Before evaluating the Ni⁰ stability under other pulse sequences, the sample was reduced again by flowing 10% H₂/He for 10 min until reaching a quasi-steady state. It is noteworthy that after the first series of pulses and further reduction, the catalyst did not ever reach 100% of Ni⁰. Despite the increase of H₂ pulse duration and further reduction of O₂ pulse duration, the second and third series of pulses with duration 20 s-O₂/40 s-H₂ (P₂) and 15 s-O₂/40 s-H₂ (P₃) still produced an increasing quantity of NiO indicating that no reversible conditions were achieved. The cyclic reversibility between Ni⁰ and NiO species was only obtained with pulse sequence of 10 s-O₂/40 s-H₂ (P₆).

It is interesting to note that for both Ni_{0.5} and Cu_{0.5} monometallic catalysts, a strong increase of water at the gas outlet compared to the blank experiment (Fig. S15, ESI) was observed under H₂ pluses, indicating that the water signal cannot be associated to the aforementioned presence of water impurities in the H₂ cylinder. Actually, the strongest detection of water occurs for pulse sequences keeping the metallic species reduced and for which no O₂ signals were detected at the gas outlet. We ascribe this behaviour as the result of O₂ adsorption followed by dissociative chemisorption which are known to be favoured on specific Cu and Ni surfaces at RT and above.⁴² It is reported that a threshold exists regarding the O₂ exposure to a metallic surface coverage leading to the formation of metal oxide islands.⁴³ When the O₂ exposure is below this threshold of oxidation, the dissociated O atoms lie just above or in the top metallic layer and can be removed by the further introduction of H₂ pulse leading to the water formation, as observed for some pulse sequences studied herein. At the opposite, for the 40 s-O₂/20 s-H₂ (P₄) or

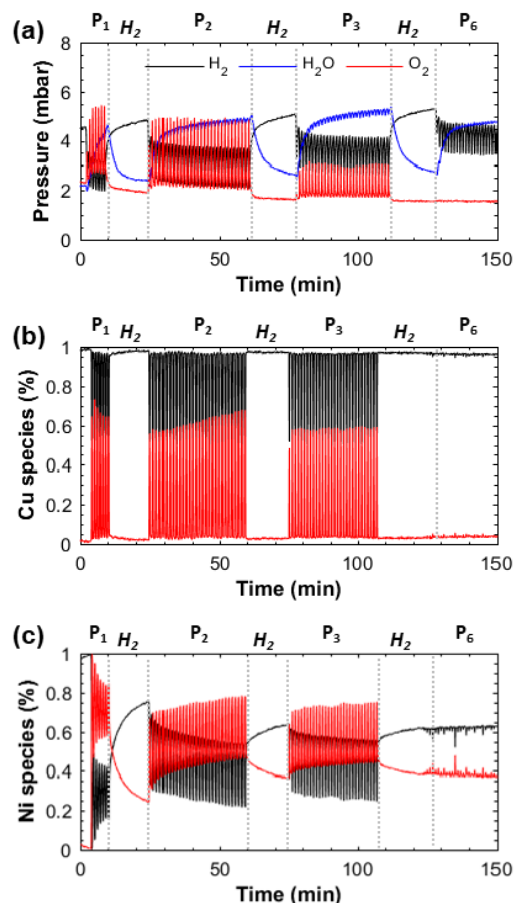


Fig. 5 Evolution of (a) H₂, H₂O and O₂ mass signals at the outlet of capillary for different pulse sequences and concentration (b) of Cu species and (c) of Ni species extracted by MCR-ALS for the Quick-EXAFS data recorded during different pulse sequences for the Ni_{0.4}Cu_{0.1} catalyst. The black lines in (b) and (c) are related to the metallic species whereas the red lines are associated to the divalent oxidic species, CuO and NiO. Pulse sequences: P₁=20 s-O₂/30 s-H₂, P₂=20 s-O₂/40 s-H₂, P₃=15 s-O₂/40 s-H₂ and P₆=10 s-O₂/40 s-H₂.

30 s-O₂/30 s-H₂ (P₅) sequences, when the O₂ exposure is higher than the oxidation threshold, Cu⁰ is oxidized into CuO at the O₂ pulse and for the latter reduced first into Cu₂O and then Cu⁰ under the H₂ pulse (Fig. S17, ESI). The amount of water formed by recombination of dissociated oxygen atoms with hydrogen and measured by MS is dependent on the quantity of M⁰ species determined by the metal speciation by MCR-ALS analysis. Namely as shown in Fig. 4, a linear correlation can be found between the average of percentages of M⁰ determined on monometallic catalysts at the different pulse sequences and the mean quantity of water formed during the pulses.

The monitoring of pulse sequences for the Ni_{0.4}Cu_{0.1} catalyst is displayed in Fig. 5. Due to the high loading in nickel for the bimetallic catalyst, the behaviour under pulse sequences was equivalent to the ones suffered by Ni_{0.5} presented in Fig. 3. The first sequences of O₂ pulses (P₁) are enough to give rise to the oxidation of Ni⁰ and Cu⁰ for sequences where no oxidation took place for Cu_{0.5}. Only, for the last pulse sequence with 10 s-O₂/40 s-H₂ (P₆), steady state conditions are achieved for Cu and Ni species with 100% of Cu⁰

and 60% of Ni⁰ and 40% of NiO. Comparison of pulse sequences carried out on the Cu_{0.1} catalyst with the one experienced by the Cu_{0.5} catalyst (Fig. S18, ESI) revealed that for the sequence 15 s-O₂/40 s-H₂ (P₃) quasi steady condition for Cu⁰ are achieved with a percentage stable around 75% and 100%, respectively, leading to dissociative chemisorption of O₂ at the surface of Cu⁰ nanoparticles. For the bimetallic sample, the same sequence gave rise to a cyclic reversible behaviour for both elements between oxidic and reduced species. This finding together with the results obtained for the Cu_{0.1} catalyst suggests that facets of nanoparticles of copper at which O₂ chemisorption is favoured are not accessible by molecular oxygen in the bimetallic catalyst. This finding suggests the formation of core-shell particles in which copper atoms are at the core and nickel ones are located in the peripheric shell resulting from the heterogeneous nucleation of Ni⁰ on Cu⁰ nuclei formed at the early stage of the reductive step of the activation.

Reaction/Regeneration Cycles

After activation of the Ni_{0.4}Cu_{0.1} catalyst, when copper and nickel are totally reduced, the ESR reaction mixture (EtOH/H₂O with He as carrier gas) was fed to the reactor at 500 °C and no re-oxidation was observed for Cu⁰ neither Ni⁰. The percentages of metallic nickel and copper species remain stable and equal to 100% during the 180 min of reaction. Fig. 6a shows the evolution of ethanol conversion with time on stream (TOS). At initial reaction times, the catalyst reaches full conversion and remains stable for ≈ 30 min. Subsequently the ethanol conversion decreases and drops to 89% after 180 min. The gaseous mixture produced during the ESR contains H₂, CO₂, CO, C₂H₄O, CH₄, and C₂H₄ (Fig. 6a). During the 30 min on stream where 100% of conversion is observed, neither CO₂ nor H₂ products keep a constant value indicating that ESR (reaction (1)) is not the only reaction occurring in the media. Side reactions such as ethanol dehydrogenation (C₂H₅OH → C₂H₄O + 2H₂), ethanol dehydration (C₂H₅OH → C₂H₄ + 2H₂O) and ethanol decomposition (C₂H₅OH → CH₄ + CO + H₂) occur as evidenced by the detection of acetaldehyde, ethylene and methane, respectively. CH₄ product displays a quasi-constant value upon TOS whereas C₂H₄O and C₂H₄, after a fast consumption at the early stage of TOS, display increasing yields upon the first 50 min to finally reach a steady value at longer TOS. Water gas shift (WGS) (CO + H₂O → CO₂ + H₂) reaction is responsible for the decrease of CO product and simultaneous increase of CO₂. The consumption of CO product could be possibly assisted by the methanation (CO + 3H₂ → CH₄ + H₂O) reaction. At TOS longer than 50 min, the parallel decrease of CO₂ and H₂ with ethanol conversion (Fig. 6a) indicates the deactivation of the catalyst for ESR. C₂H₄ and C₂H₄O have strong tendencies to form coke by ethylene decomposition (C₂H₄ → 2C + 2H₂) and/or polymerization (C₂H₄ → coke) and acetaldehyde decomposition (C₂H₄O → CH₄ + CO) followed by Boudouard reaction (2CO → C + CO₂) and methane decomposition (CH₄ → C + 2H₂).²⁰ All these reactions contribute to the rapid coke deposition observed by Raman

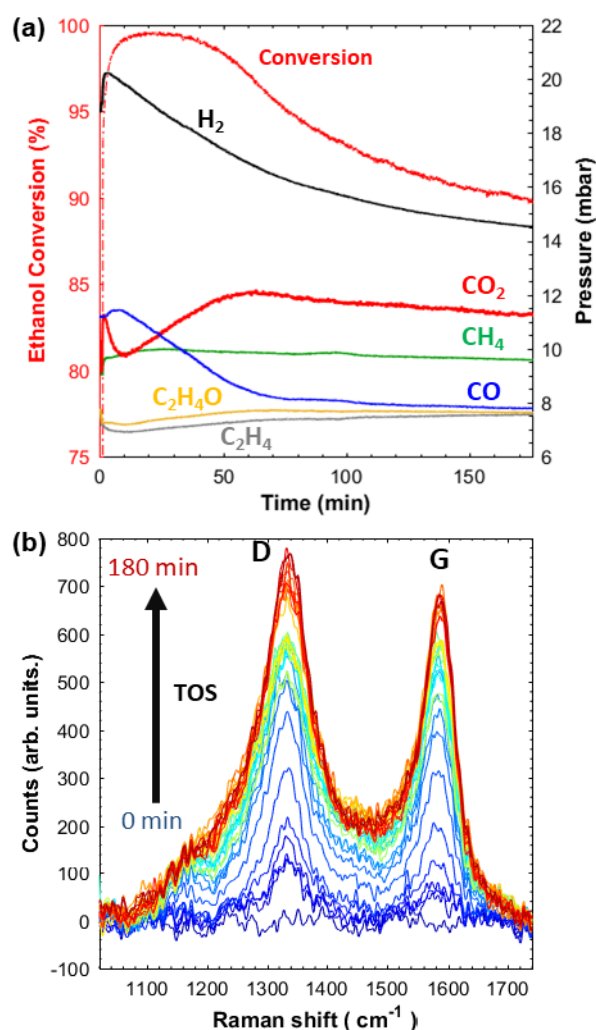


Fig. 6 (a) Evolution of (a) ethanol conversion (left axis) and products obtained during the ESR reaction monitored by MS (right axis) and (b) Raman spectra simultaneously measured during the ESR reaction on the Ni_{0.4}Cu_{0.1} catalyst.

after the contact of the catalyst with the reactants. As shown in Fig. 6b, the D line located at ~ 1336 cm⁻¹ and G line located at ~ 1586 cm⁻¹, characteristic of coke graphitic deposits, become more intense with the reaction progress.⁴⁴ The latter is characteristic of ordered graphitic carbon species such as in graphite layer and the former is indicative of large aromatic ring systems with no less than 6 fused ring but less than graphite.⁴⁵ Actually, different natures of coke are formed during ESR which do not act equivalently in catalyst deactivation.^{21,46} Filamentous coke which is formed early upon TOS does not contribute to the same extent to catalyst deactivation than graphitic and amorphous coke both encapsulating the active sites. In a recent work, Montero et al.²¹ identified the coke precursors by correlating the concentration of reaction products with the coke characteristics obtained *ex situ* by Temperature Programmed-Oxidation (TPO) and emphasized that the greater extent of acetaldehyde and ethylene reactions the greater deposition of encapsulating amorphous coke, resulting in fast deactivation. On the other hand, filamentous coke formed from CH₄ and CO

decomposition had a much lower impact on deactivation because as the metallic particles are found at the tip of the carbon filament, the active metal sites are not blocked to the reactant adsorption. Characterization of the spent catalysts, after 180 min of reaction, by microscopy fully confirms the high heterogeneous nature of the coke formed during ESR. TEM image at low resolution of the spent catalysts demonstrates the formation of carbon material with filamentary morphology together with the presence of metallic nanoparticles at the end of the filaments (Fig. 7). The high-resolution image reveals the formation of defective carbon filaments composed by misoriented graphite blocks with d-spacing of 0.345 nm characteristic of C(002) and amorphous carbon.⁴⁷ It can be also observed the encapsulation of a metallic nanoparticle inside the graphitic cages similar to a carbon onion structure⁴⁸ which is a clear evidence of the role of the coke deposition on the catalyst deactivation.

The simultaneous monitoring of reaction products with Raman spectroscopy presented herein can potentially extend the work of Montero *et al.*²¹ insofar Raman spectroscopy is very sensitive to determine the chemical nature and the graphitization order of the carbon deposited on used reforming catalysts. The Raman spectra recorded during TOS were deconvoluted into several sub-components (Fig. S19, ESI). Lorentzian functions have been used for the G and D lines.⁴⁹ The lines R1 at 1278 cm^{-1} and R2 at 1500 cm^{-1} are associated to sp^3 -rich and sp^2 - sp^3 carbon sites, and, to small aromatic rings, respectively. They are commonly associated to the presence of random amorphous carbons by opposition to the D and G lines associated to sp^2 bonds belonging to large and ordered aromatic rings.^{45,50,51} The comparison of the relative percentage of the different coke contributions with the ethanol conversion (Fig. 8) and the MS signals for CO, CH₄, C₂H₂ and C₂H₄O (Fig. 6a) clearly evidenced that the D and G lines are first formed at the early TOS with a higher amount of D-like graphitic systems. Montero *et al.*⁴⁶ described the deactivation dynamics associated to coke formation with 3 stages. The first stage is the formation of filamentous coke, which is associated herein with the high relative amount of small aromatic rings (D line) compared to the largest one (G line), with no impact on catalytic activity (Fig. 8). The ethylene and acetaldehyde produced in the same period are consumed quickly in the first minutes leading to a strong increase of CO meaning that the latter is a byproduct of acetaldehyde decomposition. But as soon as the acetaldehyde and ethylene

products start to increase their concentrations ($t > 15$ -20 min), the percentages of lines R1 and R2 characteristic of amorphous coke increase as well to reach about 30% of the coke deposits when ethanol conversion decreases (Fig. 8). At the same time, the D/G area ratio which reflects the ratio of the amounts of small and large aromatic rings decreases continuously from 2.2 to 1.4 indicating that the proportion of large graphitic-like rings increases upon TOS (Fig. 9). The increase of the level of raw absorbance of the XAS spectra (Fig. 20, ESI) measured at the advanced stage of the reaction ($t > 80$ min) indicates that the carbon deposition is still active at the time period characterizing the invariance of relative proportions of coke deposits (Fig. 8) and is responsible to the increasing decrease of ethanol conversion. The evolution of coke species obtained herein is in line with the stages 2 and 3 described by Montero *et al.*²¹ as causing severe deactivation, where the former is the formation of more condensed and graphitic coke and the latter being the one of amorphous coke fouling the catalyst surface. In our work, both stages are concomitant, the formation of graphitic and amorphous coke encapsulating the metallic sites being confirmed by the TEM images measured at the end of the reaction (Fig. 7).

The deactivated catalyst was regenerated *in situ* with introduction of 5% of O₂/He whereas the feeding into EtOH/H₂O reactants was stopped. The burning of the coke formed after 180 min of ESR reaction starts as soon as O₂ is introduced in the gas feed as evidenced by the strong increase of the signal related to production of gaseous CO and CO₂ (Fig. 10). During the first 30 min of regeneration, no change neither in the oxidation state of nickel and copper or in the intensity of the Raman lines characteristic of coke deposits was observed (Fig. 11 and Fig. S21, ESI). This is consistent with the fact that first the encapsulation of nickel and copper particles by onion-like carbon structures shown by HRTEM and/or fouling by amorphous coke protect them against oxidation and second the thickness of the coke deposits is larger than the penetration depth of the Raman excitation laser, leading to no

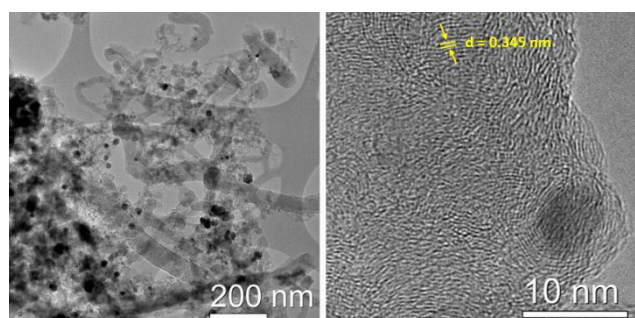


Fig. 7 TEM (left) and HRTEM (right) images of the spent Ni_{0.4}Cu_{0.1} catalyst.

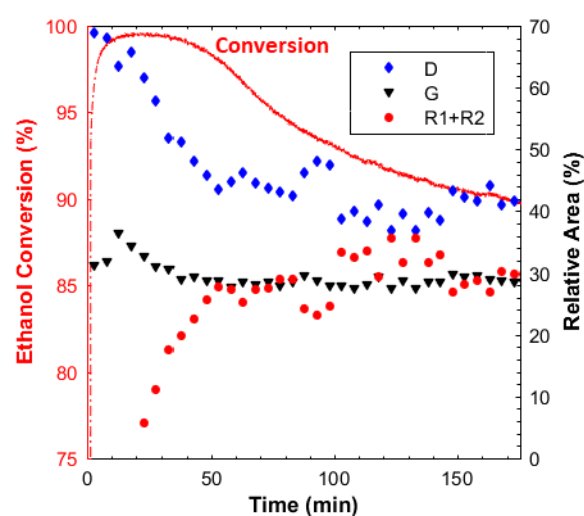


Fig. 8 Comparison as a function of TOS of the ethanol conversion with the relative area of the D, G and R₁+R₂ lines obtained by deconvolution of the Raman spectra simultaneously measured during the ESR reaction on the Ni_{0.4}Cu_{0.1} catalyst.

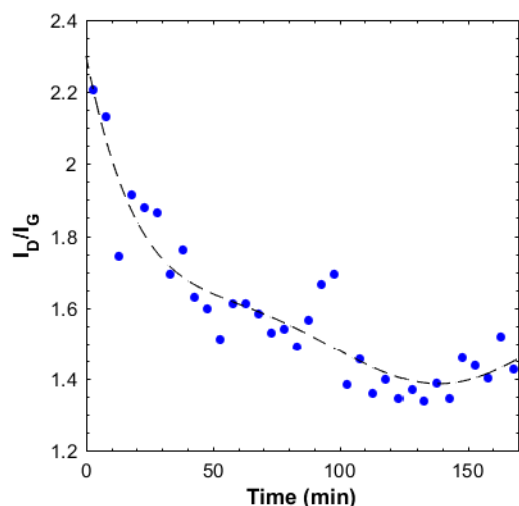


Fig. 9 Comparison as a function of TOS of the ratio between the area of the D and G lines obtained by deconvolution of the Raman spectra simultaneously measured during the first ESR reaction on the $\text{Ni}_{0.4}\text{Cu}_{0.1}$ catalyst. The line is a guide for eyes.

variation of the Raman signal at the early stage of regeneration. After 30 min of regeneration treatment, as soon as the percentages of the lines characteristic of the amorphous coke, in particular R1, start to decrease, oxidation of nickel and copper metallic species occurs quickly leading after 60 min to the transformation into NiO (80%) and $\text{CuO/Cu}_2\text{O}$ (90%) species. This is a strong evidence of the encapsulating role of the amorphous coke around nickel and copper active site responsible for the deactivation. Although D and G-like coke deposits are still dispersed at the surface of the support as evidenced by Raman spectroscopy (Fig 12), it was decided to stop the regeneration treatment and immediately restart the ethanol steam reforming reaction in order to avoid sintering of the oxidic particles. Upon re-exposure to ESR conditions, the quasi-fully oxidized metallic particles consume newly formed H_2 by the ESR reaction for recovering 80% of Ni^0 and 95% of Cu^0 after 60 min of reaction.

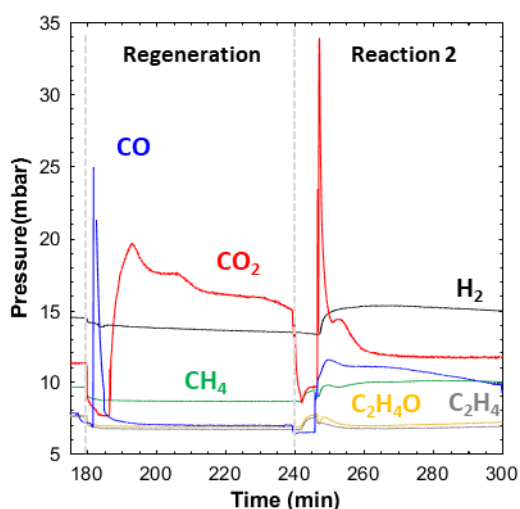


Fig. 10 Products obtained on the $\text{Ni}_{0.4}\text{Cu}_{0.1}$ catalyst during the regeneration and subsequent ESR reaction monitored by MS.

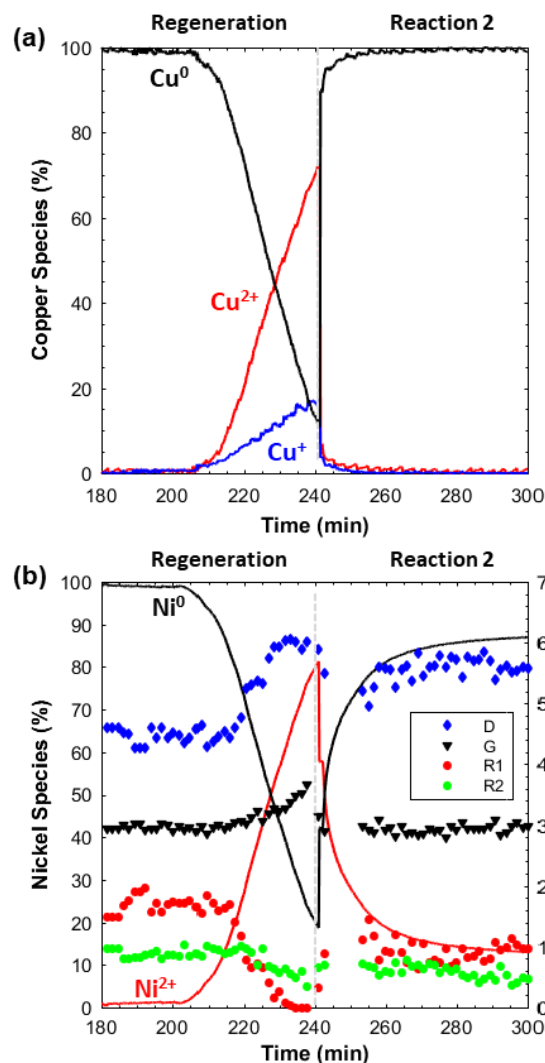


Fig. 11 Speciation of (a) copper and (b) nickel species determined by MCR-ALS analysis of the XAS data recorded during the regeneration of deactivated $\text{Ni}_{0.4}\text{Cu}_{0.1}$ catalyst and subsequent ethanol steam reforming reaction (left axis). The evolution of relative area of D, G, R1 and R2 lines determined by deconvolution of Raman spectra recorded simultaneously with the XAS data are plotted in (b) (right axis).

During the 60 min of the second ESR reaction, no deactivation was observed, ethanol conversion remained at 100%. The formation of H_2 and CO_2 are slightly higher than at the end of the first ESR reaction and stay invariant upon TOS. Selectivity towards acetaldehyde and ethylene formation is lower than at the end of the first ESR reaction and increases more slowly upon TOS (Fig. 10). Again, the comparison of the coke formed at the end of the second ESR reaction with the one formed at the end of the first reaction and at the end of regeneration (Fig. 12), clearly evidenced the change of the nature of coke deposits. The proportion of amorphous coke evaluated by sum of the relative areas of the R1 and R2 contributions is reduced by a factor 2 as described in Table S2 (ESI) and Fig. 11 at the end of the second reaction compared to the first one. This feature gives again *in situ* experimental evidence to the correlation between the amount of acetaldehyde and ethylene products and the formation of

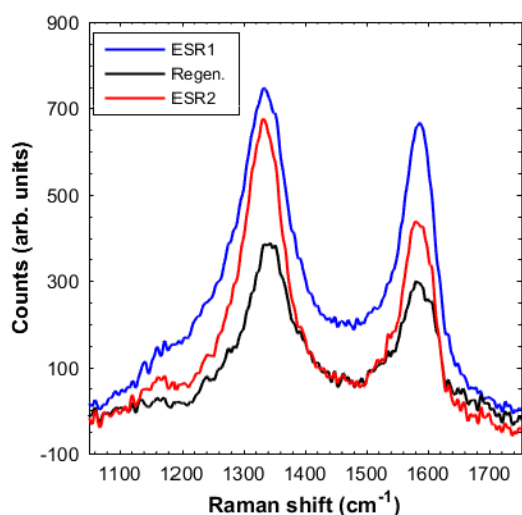


Fig. 12 Raman spectra recorded on the Ni_{0.4}Cu_{0.1} catalyst at the end of the first ESR reaction, at the end of the regeneration and at the end of the second ESR reaction.

amorphous encapsulating coke deposits.²¹ The progressive consumption of CO observed upon the second ESR reaction (Fig. 10) can be attributed to the formation of filamentous coke which has little impact on the catalyst activity since it does not block the active metal sites. As a matter of fact, the difference between the Raman spectrum recorded at the end of the second ESR reaction and the one recorded before to start the reaction is the fingerprint of the coke deposits formed upon the 60 min of second ESR reaction (Figure S22, ESI). The I_D/I_G ratio characterizing those carbonaceous species is equal to 2.48, a value which is of the same order of magnitude than the one characterizing the coke deposits formed at the early stage of reaction 1 (Stage 1 of the 3 stages described by Montero et al.⁴⁶) and which could be still associated to the formation of filamentous coke species. It is noteworthy that similar behaviours concerning products selectivity and catalyst stability after regeneration were reported for the conventional calcined catalysts prepared with the same composition.⁶ As for the catalyst studied herein, a decrease of the amount of active sites after self-reduction was observed for the conventional calcined catalyst and the recovery of catalytic activity was interpreted as a result of the Kirkendall effect occurring on the metallic nanoparticles encapsulated inside the carbon onion structures. This feature induces the fragmentation of the nanoparticles and an increase of dispersion of active sites. The Kirkendall effect appears as a driving force for the change of catalyst stability after first regeneration considering the influence of nickel particle size on the carbon formation reported in the literature, with smaller nucleation rate of carbon for smaller particle sizes.^{21,52} The effective stability of the catalyst gained upon regeneration observed for the NiCu catalyst studied herein or for the one activated conventionally⁶ (Fig S1, ESI) is strongly related to the concept of equilibrium cycle described by Montero et al.⁵³ carried out on a Ni/La₂O₃-Al₂O₃ catalyst

and consisting of a first reaction-regeneration cycle with a reaction step at 700°C necessary to obtain a catalyst which can present equivalent performances upon successive reaction-regeneration cycles.

Conclusions

Quick-EXAFS monitoring combined with MCR-ALS analysis has been unique for unraveling the intermediate species involved during the 2-step activation process of NiCu LDH-based precursors. During the oxidative step, LDH decomposition leads to the expulsion of copper from the layered edifice to form CuCl₂⁻ and atacamite-like species which are both converted into Cu⁰ species under reductive atmosphere. The conversion of NiO/NiAl₂O₄ species into Ni⁰ species resulting from the LDH decomposition and mainly formed at the early stage of the reductive step is triggered by the reduction of CuCl₂⁻ into metallic copper species. With the 2-step activation described herein, completion of nickel reduction occurs at lower temperature (455°C) than for conventional activation (500°C) and does not require long isothermal treatment as the latter. The decrease of reduction temperature of oxidic nickel species into metallic ones together with the results gained with the pulse treatment in comparison to monometallic species indicates the formation of core shell particles where copper would serve as seeds for heterogeneous nucleation of Ni⁰ species.

The simultaneous Quick-EXAFS/Mass Spectrometry and Raman spectroscopy monitoring of reaction/oxidative regeneration cycles was powerful to identify the reactant products responsible for deactivation for Ethanol Steam Reforming. Filamentous coke species formed early upon time on stream are characterized by D and G Raman lines with I_D/I_G ratio higher than 2. Deactivation starts as soon as acetaldehyde and ethylene concentration increase in the reaction media. Cracking of those products leads to the formation of encapsulating amorphous coke on the metal active surface as evidenced by the simultaneous increase of R1 and R2 lines located at 1278 and 1500 cm⁻¹, respectively. Encapsulation of active sites by this amorphous coke deposits is demonstrated by the massive reoxidation of metallic species at the advanced stage of regeneration as soon as the R1 and R2 lines disappear. Upon subsequent ESR reaction condition, the catalytic activity is restored through a self-reduction into metallic species by the H₂ product formed by ESR. The content in acetaldehyde and ethylene products remains lower than the level measured for the first reaction giving rise to an increase of catalyst stability. As a matter of fact, Raman monitoring reveals that small amount of amorphous coke is formed. Coke deposits formed by the second reaction are characterized by a I_D/I_G ratio equal to \approx 2.5. It is noteworthy that the methodology described herein can be used for all the processes aiming to produce H₂ from hydrocarbon feedstocks such as steam reforming of methane today used for \sim 50% production of H₂ worldwide,⁵⁴ provided of course that the pressure condition necessary for such kind of relevant industrial processes has been reached. Recent developments

of reactors used for XAS to study reactions under high pressure^{31,55} clearly evidence that the pressure gap to use similar methodology to better understand activation, deactivation and regeneration of steam reforming catalysts is not so far to be overcome.

Finally, as a perspective of this work, a new regeneration strategy based on the alternate use of oxidative and reductive gas pulses at 500°C on spent catalysts could be investigated in order to avoid the full reoxidation of metallic active species upon oxidative regeneration as observed herein. The oxidative pulses would be used to burn coke deposits whereas the reductive ones would be provided to prevent the oxidation of metallic nanoparticles possibly occurring during the oxidative pulse. The best pulse conditions could be optimized according to the behaviour observed on freshly activated catalysts as carried out in this work.

Conflicts of interest

There are no conflicts to declare.

Acknowledgements

This work was supported by the CAPES, CNPq (grant number 201653/2015-0), FAPESP and by a public grant overseen by the French National Research Agency (ANR) as a part of the “Investissements d’Avenir” program (ref: ANR-10-EQPX-45). We acknowledge SOLEIL Synchrotron for providing beamtime at the ROCK beamline. The authors also acknowledge LNNano/CNPEM for technical support during electron microscopy work. The authors also acknowledge Thomas Putaud for the Matlab® functions for the deconvolution of the Raman spectra.

References

- 1 F. Wang, Y. Li, W. Cai, E. Zhan, X. Mu and W. Shen, *Catal. Today*, 2009, **146**, 31–36.
- 2 J. M. R. Gallo, J. M. C. Bueno and U. Schuchardt, *J. Braz. Chem. Soc.*, 2014, **25**, 2229–2243.
- 3 S. Velu, N. Satoh, C. S. Gopinath and K. Suzuki, *Catal. Letters*, 2002, **82**, 145–152.
- 4 S. D. Davidson, H. Zhang, J. Sun and Y. Wang, *Dalt. Trans.*, 2014, **43**, 11782–11802.
- 5 W. H. Cassinelli, L. Martins, A. R. Passos, S. H. Pulcinelli, A. Rochet, V. Briois and C. V. Santilli, *ChemCatChem*, 2015, **7**, 1668–1677.
- 6 A. R. Passos, S. H. Pulcinelli, C. V. Santilli and V. Briois, *Catal. Today*, 2019, **336**, 122–130.
- 7 C. Zhang, P. Zhang, S. Li, G. Wu, X. Ma and J. Gong, *Phys. Chem. Chem. Phys.*, 2012, **14**, 3295–3298.
- 8 G. Fan, F. Li, D. G. Evans and X. Duan, *Chem. Soc. Rev.*, 2014, **43**, 7040–7066.
- 9 T. Baskaran, J. Christopher and A. Sakthivel, *RSC Adv.*, 2015, **5**, 98853–98875.
- 10 W. Y. Hernández, J. Lauwaert, P. Van Der Voort and A. Verberckmoes, *Green Chem.*, 2017, **19**, 5269–5302.
- 11 A. I. Khan and D. O’Hare, *J. Mater. Chem.*, 2002, **12**, 3191–3198.
- 12 F. Prinetto, G. Ghiotti, P. Graffin and D. Tichit, *Microporous Mesoporous Mater.*, 2000, **39**, 229–247.
- 13 Y. Tokudome, N. Tarutani, K. Nakanishi and M. Takahashi, *J. Mater. Chem. A*, 2013, **1**, 7702–7708.
- 14 V. Oestreicher and M. Jobbágy, *Langmuir*, 2013, **29**, 12104–12109.
- 15 A. E. Gash, T. M. Tillotson, J. H. Satcher, J. F. Poco, L. W. Hrubesh and R. L. Simpson, *Chem. Mater.*, 2001, **13**, 999–1007.
- 16 A. Alexandre, F. Medina, X. Rodriguez, P. Salagre, Y. Cesteros and J. E. Sueiras, *Appl. Catal. B Environ.*, 2001, **30**, 195–207.
- 17 F. Cavani, F. Trifirò and A. Vaccari, *Catal. Today*, 1991, **11**, 173–301.
- 18 H. W. P. Carvalho, S. H. Pulcinelli, C. V. Santilli, F. Leroux, F. Meneau and V. Briois, *Chem. Mater.*, 2013, **25**, 2855–2867.
- 19 M. Ferrandon, V. Daggupati, Z. Wang, G. Naterer and L. Trevani, *J. Therm. Anal. Calorim.*, 2015, **119**, 975–982.
- 20 L. V. Mattos, G. Jacobs, B. H. Davis and F. B. Noronha, *Chem. Rev.*, 2012, **112**, 4094–4123.
- 21 C. Montero, A. Remiro, B. Valle, L. Oar-Arteta, J. Bilbao and A. G. Gayubo, *Ind. Eng. Chem. Res.*, 2019, **58**, 14736–14751.
- 22 K. V. Manukyan, A. J. Cross, A. V. Yeghishyan, S. Rouvimov, J. J. Miller, A. S. Mukasyan and E. E. Wolf, *Appl. Catal. A Gen.*, 2015, **508**, 37–44.
- 23 D. M. Argyle and H. C. Bartholomew, *Catalysts*, 2015, **5**, 145–269.
- 24 A. R. Passos, C. La Fontaine, L. Martins, S. H. Pulcinelli, C. V. Santilli and V. Briois, *Catal. Sci. Technol.*, 2018, **8**, 6297–6301.
- 25 H. Wang, C. Chen, Y. Zhang, L. Peng, S. Ma, T. Yang, H. Guo, Z. Zhang, D. S. Su and J. Zhang, *Nat. Commun.*, 2015, **6**, 1–6.
- 26 A. Rochet, B. Baubet, V. Moizan, E. Devers, A. Hugon, C. Pichon, E. Payen and V. Briois, *J. Phys. Chem. C*, 2015, **119**, 23928–23942.
- 27 W. H. Cassinelli, L. Martins, A. R. Passos, S. H. Pulcinelli, C. V. Santilli, A. Rochet and V. Briois, *Catal. Today*, 2014, **229**, 114–122.
- 28 Y. Tokudome, K. Nakanishi, K. Kanamori and T. Hanada, *J. Colloid Interface Sci.*, 2010, **352**, 303–308.
- 29 C. La Fontaine, L. Barthe, A. Rochet and V. Briois, *Catal. Today*, 2013, **205**, 148–158.
- 30 V. Briois, C. La Fontaine, S. Belin, L. Barthe, T. Moreno, V. Pinty, A. Carcy, R. Girardot and E. Fonda, in *Journal of Physics: Conference Series*, 2016, vol. 712, pp. 012149–012155.
- 31 C. Lesage, E. Devers, C. Legens, G. Fernandes, O. Roudenko and V. Briois, *Catal. Today*, 2019, **336**, 63–73.
- 32 A. de Juan, J. Jaumot and R. A. Tauler, *Anal. Methods*, 2014, **6**, 4964–4976.
- 33 Y. J. Liu, T. Tran, G. Postma, L. M. C. Buydens and J. Jansen, *Anal. Chim. Acta*, 2018, **1020**, 17–29.

- 34 H. W. P. Carvalho, F. Leroux, V. Briois, C. V. Santilli and S. H. Pulcinelli, *RSC Adv.*, 2018, **8**, 34670–34681.
- 35 J. Jaumot, A. de Juan and R. Tauler, *Chemom. Intell. Lab. Syst.*, 2015, **140**, 1–12.
- 36 H. R. Keller and D. L. Massart, 1992, **32**, 209–224.
- 37 S. J. Gregg and K. S. W. Sing, *Adsorption, surface area and porosity*, Academic Press, London, 1997, vol. 2.
- 38 S. Jaeger, S. F. Zawadzki, A. Leuteritz and F. Wypych, *J. Braz. Chem. Soc.*, 2017, **28**, 2391–2401.
- 39 V. Briois, C. Cartier, M. Verdaguer, R. M. Lequan, M. Lequan, G. Van der Laan and A. Michalowicz, *Chem. Mater.*, 1992, **4**, 484–493.
- 40 J. Brugger, B. Etschmann, W. Liu, D. Testemale, J. L. Hazemann, H. Emerich, W. van Beek and O. Proux, *Geochim. Cosmochim. Acta*, 2007, **71**, 4920–4941.
- 41 C. Ruckebusch, A. De Juan, L. Duponchel and J. P. Huvenne, *Chemom. Intell. Lab. Syst.*, 2006, **80**, 209–214.
- 42 F. Besenbacher and J. K. Nørskov, *Prog. Surf. Sci.*, 1993, **44**, 5–66.
- 43 Y. Xu and M. Mavrikakis, *Surf. Sci.*, 2001, **494**, 131–144.
- 44 F. Tuinstra and J. L. Koenig, *J. Chem. Phys.*, 1970, **53**, 1126–1130.
- 45 X. Li, J. ichiro Hayashi and C. Z. Li, *Fuel*, 2006, **85**, 1509–1517.
- 46 C. Montero, A. Ochoa, P. Castaño, J. Bilbao and A. G. Gayubo, *J. Catal.*, 2015, **331**, 181–192.
- 47 T. V Reshetenko, L. B. Avdeeva, Z. R. Ismagilov, V. V Pushkarev, S. V Cherepanova, A. L. Chuvilin and V. A. Likholobov, *Carbon N. Y.*, 2003, **41**, 1605–1615.
- 48 F. Banhart, P. Redlich and P. M. Ajayan, *Chem. Phys. Lett.*, 1998, **292**, 554–560.
- 49 A. Lazzarini, A. Piovano, R. Pellegrini, G. Leofanti, G. Agostini, S. Rudić, M. R. Chierotti, R. Gobetto, A. Battiato, G. Spoto, A. Zecchina, C. Lamberti and E. Groppo, *Catal. Sci. Technol.*, 2016, **6**, 4910–4922.
- 50 S. Mahamulkar, K. Yin, P. K. Agrawal, R. J. Davis, C. W. Jones, A. Malek and H. Shibata, *Ind. Eng. Chem. Res.*, 2016, **55**, 9760–9818.
- 51 P. Kim, A. Johnson, C. W. Edmunds, M. Radosevich, F. Vogt, T. G. Rials and N. Labbé, *Energy and Fuels*, 2011, **25**, 4693–4703.
- 52 H. S. Bengaard, J. K. Nørskov, J. Sehested, B. S. Clausen, L. P. Nielsen, A. M. Molenbroek and J. R. Rostrup-Nielsen, *J. Catal.*, 2002, **209**, 365–384.
- 53 C. Montero, A. Remiro, A. Arandia, P. L. Benito, J. Bilbao and A. G. Gayubo, *Fuel Process. Technol.*, 2016, **152**, 215–222.
- 54 S. Chen, C. Pei and J. Gong, *Energy Environ. Sci.*, 2019, **12**, 3473–3495.
- 55 A. Aguilar-Tapia, S. Ould-Chikh, E. Lahera, A. Prat, W. Delnet, O. Proux, I. Kieffer, J. M. Basset, K. Takanabe and J. L. Hazemann, *Rev. Sci. Instrum.*, , DOI:10.1063/1.4998929.